Flexible flapping wing in hover flight

Leblanc Marion, Le Creurer Nicola, Maqueda Muñoz Alejandro, Moura Raquel, and Shaik Sajeed Hussain

Abstract

Fruit flies, along with other animal species such as hummingbirds, use fluid-structure interaction to their advantage, as it allows them to increase the generation of propulsive force whilst reducing power consumption. This interaction is studied by approximating a fruit fly's wings in hovering flight mode, with a flat plate, and conducting simulations using diverse meshing techniques that allow morphing solvers to be used. The evolution of lift and drag coefficients, C_L and C_D will be compared with the reference paper.

Nomenclature

C_p = pressure coefficient
C_L = lift coefficient
C_D = drag coefficient
c = chord (m)
ρ_s = wing density (kg/m^3)
ρ_f = air density (kg/m^3)
h(t) = plunge motion (m)
h_a = motion amplitude (m)
f = frequency of the motion (Hz)
f1 = natural frequency of the plate (Hz)
k = reduced frequency
t^* = time dimensionless parameter
U = reference velocity (m/s)
f1 = first natural frequency of the wing
Δx = mesh size (m)
Δt = step time (m)

I. Introduction

The fruit fly wings are flexible and deform substantially during flight. Hence, in this system the aerodynamic, structural, and flight dynamics are strongly coupled and nonlinear; making it an interesting movement to study.

Flyers, especially those that operate at very low Reynolds ($Re = 100$), like fruit flies ([1, 2]), maintain the flight by taking advantage of unsteady mechanisms such as: clapping and flinging, creating a delayed stall by prolonging leading-edge vortices (LEVs), capturing the wake of a wing during the return stroke and using rotational forces resulting from both pitching and plunging movements. Furthermore, the flexible wing pitch and plunge during flight reduce the power consumption by enhancing the propulsive force generated.

The objective of this work is to simulate the plunging movement of the wing and study the fluid-structure interaction following the work of Sridhar and Kang [1] and [3]. The deformation of the plate is an important aspect as the three meshes needed to properly discretize it: a static mesh, a dynamic mesh, and a mesh inside the solid plate that represents the wing. With a $Re = 100$ characteristic of the fruit fly flight, the flow is laminar, and without any need for a turbulence model, the Navier-Stokes equations are directly solved.

II. Problem description and Methods

A. Physical Modelling choices and justifications

In this study, the fruit fly wing is modeled as a homogeneous elastic flat of a unit chord, a span of 0.25 m with a uniform thickness of 1.5 mm. The only motion considered is the plunging of the leading edge, any stroke deviation angle or torsion motion is neglected. As mentioned, this model is not fully representative of reality, but the 3D effects coming from spanwise deformation can be neglected as such Reynolds numbers. In our case, a pseudo-2D simulation is sufficient to only have the chordwise flexibility [4].

The fluid-structure interaction of flexible wings is characterized by the density ratio $\rho* = \rho_s/\rho_f = 1000\ \mathrm{kg/m^3}$, where $\rho_s = 1200\ \mathrm{kg/m^3}$ is the wing density and $\rho_f = 1.2\ \mathrm{kg/m^3}$ is the density of the air.

B. Meshes

Three meshes need to be generated to fully understand the plunging motion and its effects on the vortices in the wake. A mesh for the solid plate, an overset mesh that moves with the motion, and a static mesh are needed. As a pseudo-2D simulation is performed, all three meshes have only one cell in the span direction. This section will present the choices made in the meshing process.

1. Plate Mesh

To see the effect of the hovering motion on the structure, the interior of the flexible plate needs to be meshed. The plate dimensions are mentioned in the previous section II A. The plate mesh is done using StarCCM+, using a directed mesh. This option allows the sweep of the mesh from one source surface to a target surface, choosing the number of layers needed. In this case, these two surfaces are the sides of the plate since a unique cell is required for the span. Following the work of [1], 51 nodes are targeted on the plate chord, thus a base size, and a target surface size of $1/51 = 0.02$m. A quadrilateral mesh is used.

Along the thickness of the plate, two cells are sufficient for the simple plunging motion considered. For a more complex motion like torsion, more cells would have been needed. The following Figure 1 presents the mesh used for the solid plate:

2. Overset Mesh

When meshing a moving part, it is useful to build an overset mesh along with a static mesh. The first one, moving along with the solid part is usually quite refined, since the movement will involve a more complex flow around the plate. Thus, it is limited to a small part of the domain, around the solid. The second mesh (static) is describing the whole computational domain and is usually quite coarse. The two computational grids overlap each other, allowing an exchange of flow

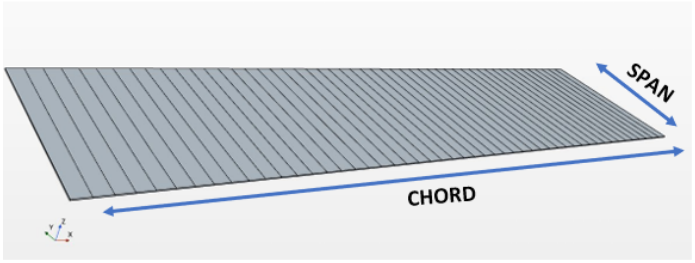

Fig. 1: Plate mesh and geometry

field information during simulations.

As for the plate mesh, a directed mesh was used in StarCCM+ to sweep from one wall of the domain (source surface) to the other (target surface). A quadrilateral mesher was used, with a base size of 0.1m. Three surface controls were implemented. First, a target surface size of $7.5 \cdot 10^{-4} m$ was imposed at the leading and trailing edges, since only two cells are wanted in the thickness of the plate. The second one is to control the mesh on the top and bottom surfaces of the plate with a target surface size = 0.0025m to have a refined mesh of 400 cells. The last surface control is for the walls of the overset mesh with a target surface size of 0.035 m. This allows for a continuity in the cell size between the overset and the static mesh. In doing so, an O-mesh is constructed, where the cell sizes at the boundaries with the static mesh are kept constant, while the growth rate can be refined.

Many configurations of dimensions were tested for the overset mesh because this choice influences highly the computational time, the convergence of the simulation, the refinement, etc (details in section II E). The final dimensions were set to 1 chord before and after the solid part in length, and 3 chords in height. The following Figures 2 and 3 present the meshing of the overset domain, with a zoom on the leading edge of the plate where two cells are imposed.

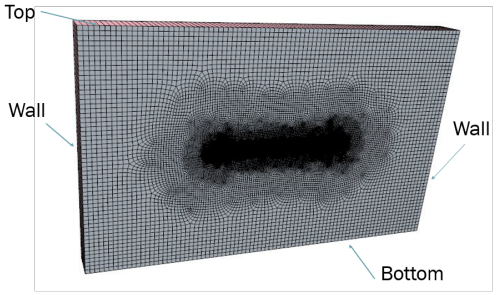

Fig. 2: Overset mesh

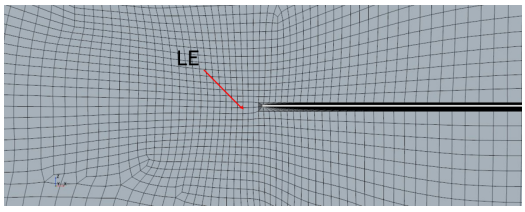

Fig. 3: Zoom around the leading edge of the plate

The chosen dimensions ensure that the plate never reaches a state where it is not within the overset mesh, allowing it to always capture the flow around the moving plate with the morphing overset mesh.

3. Static Mesh

The last mesh to build is the static mesh. It represents the entire computational domain, hence it is coarser than the overset mesh. The dimensions have to be a compromise between small enough to reduce computational time and high enough to neglect the effects of the walls in our flow field. As well, the whole amplitude of movement needs to be contained in the static domain.

Like before, a directed mesh was used in StarCCM+, sweeping from one wall of the domain (source surface) to the other (target surface). The base of the quadrilateral mesher is 0.3m. A refinement block (volumetric control) is defined at the location of the overset mesh. As the cells from the two grids overlap during motion, mesh convergence issues can arise if their sizes are too different. Thus, the target surface size at the interface is set to 0.035m to have a smooth transition between the overset and the static mesh. The final dimensions of the static mesh are 5 chords in front and after the plate in length, and 10 chords in height.

Figure 4 presents the static mesh. The refinement block at the location of the overset mesh can be seen.

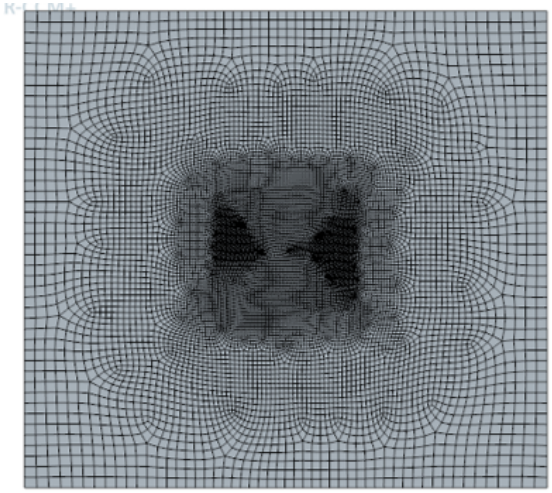

Fig. 4: Static mesh

C. Models, Numerical schemes and Boundary Conditions

This section will introduce the models, numerical schemes, and boundary conditions used in the simulations of this study.

Two different models are defined, one for the fluid part (air), and one for the solid part (plate). The air is modelled by a gas of constant density $\rho_f = 1.18415 kg/m^3$, and dynamic viscosity $\mu = 1.855 \cdot 10^{-5} Pa.s$. The reference pressure is 101325 Pa. The flow is incompressible, thus a segregated flow model is selected. Considering the low Reynolds number and the unsteadiness of this problem, the laminar and implicit unsteady model options are chosen. In StarCCM+, solving for laminar flows means that no turbulence model is selected, and thus the full Navier-Stokes equations are solved.

For the solid part, an aluminum plate with a Young Modulus of $5 \cdot 10^9$ Pa is used. The models selected are implicit unsteady and isotropic linear elasticity.

There is no incoming flow because of the hovering flight, so the theoretical velocity initial condition is 0 m/s. In reality, it was set to 10^{-4} m/s, so that no simulation issues are encountered. The initial pressure is 0 Pa, because of the definition of the reference pressure.

As for boundary conditions, a stagnation inlet and a pressure outlet are defined. All other parts are considered as walls, with a slip condition imposed on the plate surface. An overset boundary condition is set at the interface between the static and overset meshes.

The solid stress solver is used to solve for deformations within the solid plate. Also, the mesh morpher solver is chosen to keep the deformations of the meshes under control. The mesh morphing allows the computational mesh to move in a way that preserves its quality when a boundary moves. The Fluid-Structure coupling solver is selected which acts as a two-way coupling between solid deformations and the fluid solver. At each time, the interactions between fluid and structure are computed until sufficient convergence is reached for the displacement of the flexible plate within the inner iteration before advancing to the next time step.

D. Plunge Motion

To model the movement of the wing, a harmonic plunge motion is imposed at the leading edge of the plate, using the methodology followed in [1, 3]:

$$h(t) = h_a \cdot sin(2\pi f t) \tag{1}$$

where h_a is the motion amplitude and f the frequency of the signal. As the incoming velocity is zero, the maximum translational velocity at the leading edge, U, is taken as a reference. The value of U is directly obtained by taking the derivative of Equation 1, $U = 2\pi f h_a$. Hence, the reduced frequency in hover flight becomes $k = \pi f c/U = c/(2h_a)$. The Strouhal number is $St \approx f h_a/U = 1/(2\pi)$.

The plunging motion has two degrees of freedom and can be univocally determined by the values of h_a and f. Equivalently, one can fix $h(t)$ by choosing a value for the reduced frequency, k, and for the frequency ratio, f/f_1, where f_1 is the natural oscillation frequency of the plate. Following the study conducted in [1], the values of the reduced frequency will be taken in the interval $k \in [0.1, 3]$. The frequency ratio for fruit flies is limited to 0.8, hence $f/f_1 < 0.8$ will be taken in this study.

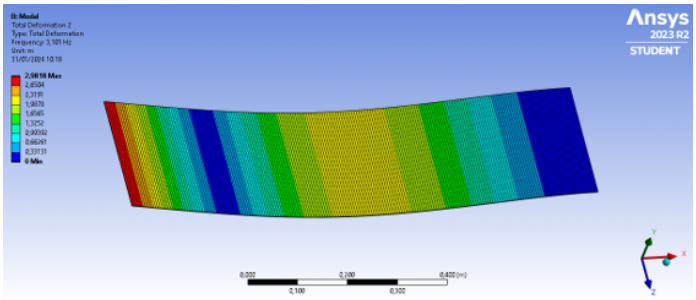

Fig. 5: Computation of f1

Using Ansys, the natural frequency of the plate is computed (Figure 5), resulting in a value of $f_1 = 0.4$ Hz. To try to reproduce the results for the configuration yielding the maximum efficiency

([1, 4]), η, the reduced frequency is taken as $k = 0.3$, and the frequency ratio is chosen to be $f/f_1 = 0.35$.

Thus, the frequency of motion is equal to $f = 0.14Hz$, the period of oscillations is $T = 1/f = 7.14s$ and the reference velocity is $U = 1.47m/s$.

E. Problems encountered and solution tested

This section will present the difficulties faced when configuring the meshes and implementing simulations. The first idea was to use the software ICEM to build the three meshes because it allows to easily control the cell sizes. Also, there is the possibility to extrude a 2D into a 3d mesh while imposing only one cell in the spanwise direction, which was not as simple in StarCCM+. However, the plunge motion specification needs to be fixed to a surface in StarCCM+, thus the meshing of the plate needs to be done using that same software. Still, at high amplitudes of motion, small cells from the overset mesh were overlapping bigger cells from the static mesh, causing the simulations to crash. Another issue was the apparition of negative volume cells around the plate during the simulation. To solve those problems, many solutions were tested. First, multiple refinements of the overset mesh were performed, in size and number of cells around the plate. A balance had to be found between an overset mesh too small causing problems at the interfaces during the motion, and a mesh too big which could not be as refined because of the high computational time it would cause. Another solution tested was to delete the static mesh while changing the boundary conditions of the overset mesh so that any problem with interfaces would not appear. However, this solution is very costly as the overset mesh has to be increased in size. Finally, the solution presented in this report, and the only one that ran, was to implement a 0-mesh in StarCCM directly, without using ICEM.

F. Mesh convergence study

To be sure that the results of the simulations are trustable and accurate, mesh independence and time independence studies need to be performed. It ensures that the mesh cell sizes and the time step do not act as variables in the results obtained.

1. Time independence study

The time step is computed using the following formula:

$$CFL = U \cdot \frac{\Delta t}{\Delta x} \tag{2}$$

With Δx, the smallest size in the mesh (thickness/2 = 0.00075 m). For a value of CFL = 1, it yields $\Delta t = 5.1 \cdot 10^{-4} s$. The values of $\overline{C_L}$ and $\overline{C_D}$, the time-averaged coefficients of C_L and C_D, are selected to evaluate the time convergence. Their frequencies are also analyzed by performing an FFT on the signals. The resulting forces in this study are not exactly periodic in time, so to have a representative and avoid any initial transient effects, the mean coefficients are computed over a few periods. The value of the time step is increased, by choosing higher CFL numbers. The following table 1 presents the different time steps that were tested:

No trend can be identified for mean Cl, Cd, and the respective frequencies. Hence, no conclusions can be taken from the time-step convergence study. Moreover, for CFL numbers 1 and 10, the results obtained were not physical, as they presented substantial fluctuations, and consequently were not

CFL	1	10	25	50	75	100
Time Step (s)	$5.1 \cdot 10^{-4}$	$5.1 \cdot 10^{-3}$	0.01275	0.0255	0.03825	0.051
$\overline{C_L}$			0.0562	-0.0203	-0.0668	0.0921
FFT C_L Frequency			0.1380	0.1375	0.1315	0.1406
$\overline{C_D}$			-0.7078	-1.4287	-1.2608	-1.2726
FFT C_D Frequency			0.2842	0.2750	0.2630	0.2813

Table 1: Time convergence

taken into account. The mean CL number is approximately zero which varies from the results expected from Sridhar and Kang's paper. Nonetheless, the frequencies of CL and CD are expected: 0.14 for CL same frequency of the plunge motion and pair vortex shedding, and double, 0.28, for CD, as each vortex contributes positively to the drag.

The following figure 6 shows the evolution of $\overline{C_L}$ along time, at two different CFLs. The mean is zero.

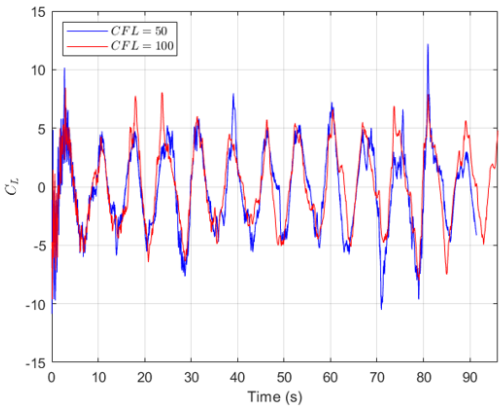

Fig. 6: $\overline{C_L}$ signal over time

2. Mesh independence study

The mesh convergence study is performed even if it is not possible to determine the optimal time step with the time convergence study. The minimum value at which results can be exploited is used, hence CFL = 25. The mesh convergence only focuses on the overset mesh growth rate, looking at $\overline{C_L}$ and $\overline{C_D}$ values, and their respective frequency.

Growth rate	1.04	1.06	1.08	1.12	1.15
$\overline{C_L}$	0.0562	-0.0071	0.0154	-0.0185	-0.0516
FFT C_L Frequency	0.1380	0.1378	0.1429	0.1400	0.1429
$\overline{C_D}$	-0.7078	-0.7529	-0.7664	-0.7707	-0.7826
FFT C_D Frequency	0.2842	0.2833	0.2778	0.2818	0.2769

Table 2: mesh convergence

The following Figures 7 and 8 present the overset mesh with a finer mesh (growth rate of 1.04), and a coarser mesh (growth mesh of 1.15).

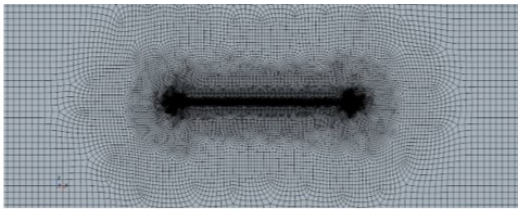

Fig. 7: growth rate = 1.04

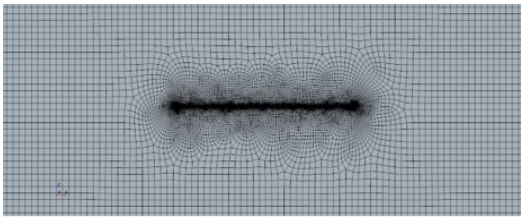

Fig. 8: growth rate = 1.15

No trend of mean CL, CD, and respective frequencies can be identified. Hence, the mesh convergence study is inconclusive. As it happened for the time step convergence study the mean CL is zero, however the frequencies are physically correct. The mean CD is negative indicating propulsion.

3. Mesh and CFL choice and justification

Since the mesh and time step convergence studies were inconclusive the mesh and CFL chosen were the more conservative: growth rate = 1.04 and CFL = 25. This mesh is fine enough to have a fine mesh in a vortex shed, as seen in Figure 9

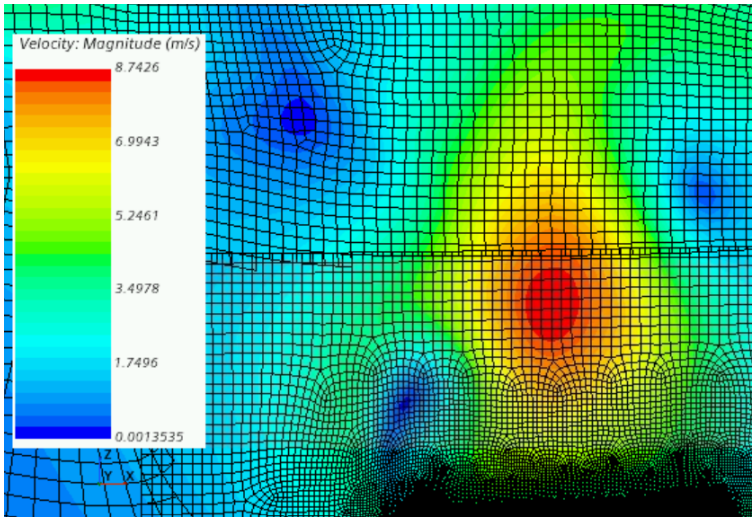

Fig. 9: Vortex spatial discretization.

III. Solutions

In the previous sections, the results obtained from numerical simulations using the solid stress solver implemented in STARCCM+ in the framework of linear elasticity have been exposed. In this section, we discuss how several observations allow us to conclude that this model is not suitable for the simulation of the problem in question, showing how the modification of the structural problem approach allows us to obtain coherent results. This coherence is verified thanks to the comparison with what has been observed in other studies, as well as what is expected from the theoretical analysis of the case.

A. Comparison between hyperelastic and linear elasticity simulations.

The convergence analyses of both mesh and Courant numbers have been performed under the hypothesis of linear elasticity, for the case of reduced frequency $k = 0.3$ and amplitude $h_a = 1.67m$. The simulations show a very strong deformation of the plate when the motion starts, with an increase of the chord length of the plate of more than 80% at $t^* = 0.25$ and $t^* = 0.75$. Such deformations are not expected for the case under study, as experimental observations of similar cases only indicate bending deformations.

In addition, the observed bending is clearly outside the range of linear elasticity, with pitch angles of up to 150^o being obtained (see Figures 11 and 13). Note that the pitch angle is defined in the following formulas as the angle between the vertical and the plate, consistent with the motion of a fruit fly wing (see Figure 10). The approximation shown in the figure is validated by high-fidelity solutions of deformable wing motion by Kang C. *et al* in [3], and is computed by translating the structural deformation into pitch angle and solving the equation

$$\alpha_{passive} = 90^o - \alpha_a cos(2\pi t^* + \psi), \tag{3}$$

where

$$\begin{cases} \alpha_0 = atan[y_{TE}(t^* = 0) - y_{LE}(t^* = 0)] \\ \alpha_{0.25} = atan[y_{TE}(t^* = 0.25) - y_{LE}(t^* = 0.25)] \end{cases} \tag{4}$$

are the measured pitch angles at the beginning and first quarter of the flapping period motion.

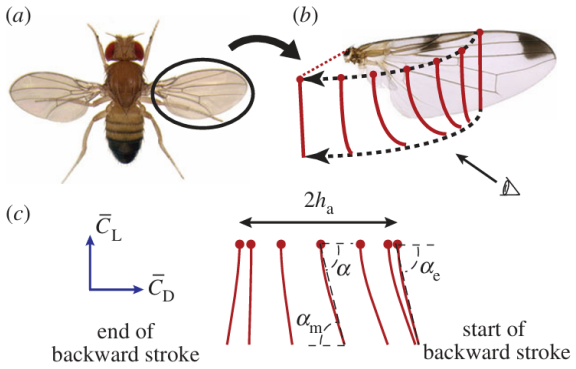

Fig. 10: Pitch angle definition for the flapping motion of the fruit fly wing.

On the basis that the biological material of which insect wings are made can be considered as a hyperelastic material, it is necessary to abandon linear elasticity models, which allows us to obtain more coherent results that coincide with those reported in [1] and [3]. For this purpose, the neo-Hookean model implemented in StarCCM+ is used. The inputs of this model are computed based on the chosen elastic modulus (E=5 GPa), thanks to the isotropic material hypothesis.

Figure 13 and 14 show the fluid velocity field and the plate deformation at four characteristic points of the cycle. It can be seen how the implementation of the non-linear model makes the pitch angle significantly lower, as well as avoiding the increase in the length of the plate chord.

The pitch measurement and the approximation by its first harmonic are shown in Figure 12 for the hyperelastic case.

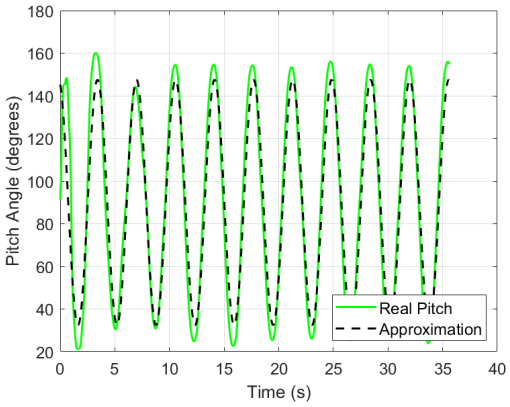

Fig. 11: Pitch angle obtained with linear elasticity assumption.

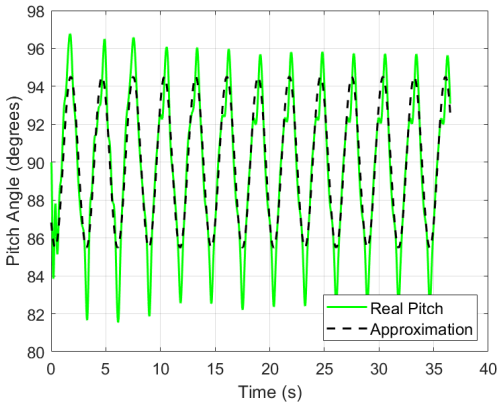

Fig. 12: Pitch angle obtained with hyperelastic assumption.

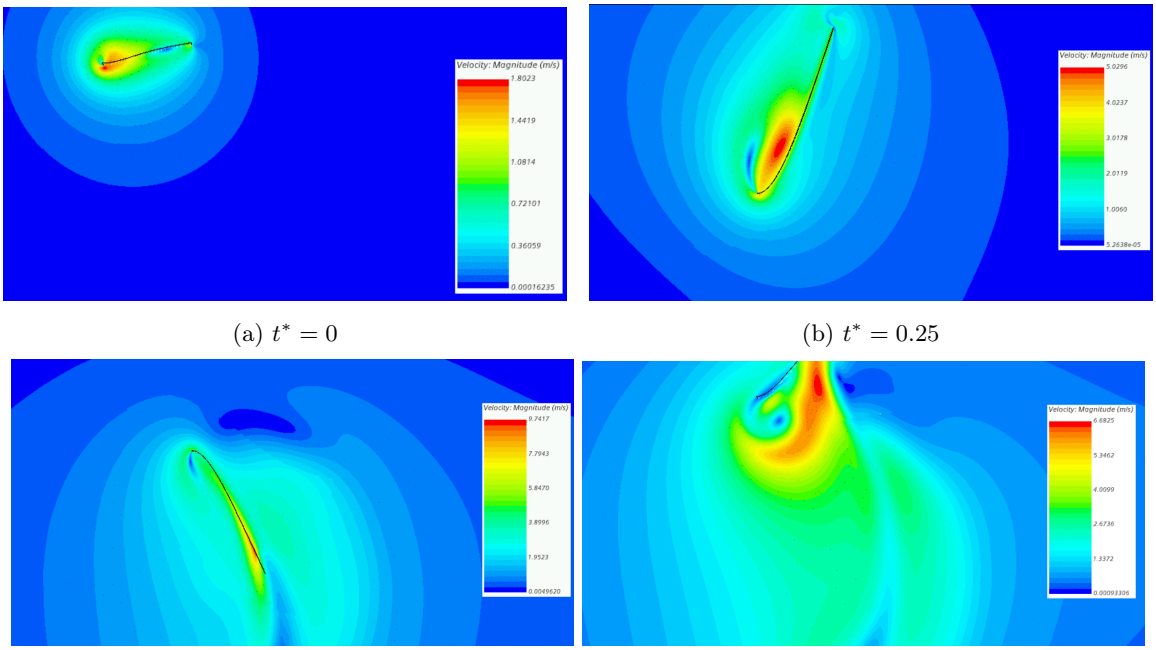

(a) $t^* = 0$

(b) $t^* = 0.25$

(c) $t^* = 0.75$

(d) $t^* = 1$

Fig. 13: Velocity field obtained with the linear elasticity assumption.

The difference between the two simulations is more evident when the average aerodynamic coefficients are analyzed once the simulations go beyond the transient state. One of the problems discussed above and related to the linear approach to the elastic problem is that the average lift coefficient obtained over a period is zero (Figure 19). To explain this phenomenon, the fluid field along the plate motion observed with this type of simulation can be considered. When the leading edge begins to descend, a suction zone is generated at the top as a consequence of the appearance of a strong vortex that accelerates the fluid and decreases its static pressure. When the plate rises, vorticity is not generated with the same intensity in the lower part as a consequence of the large bending and deformation of the plate, so no negative lift is generated in that path. However, when the leading edge reaches the initial position again, the inertia of the trailing edge causes the plate

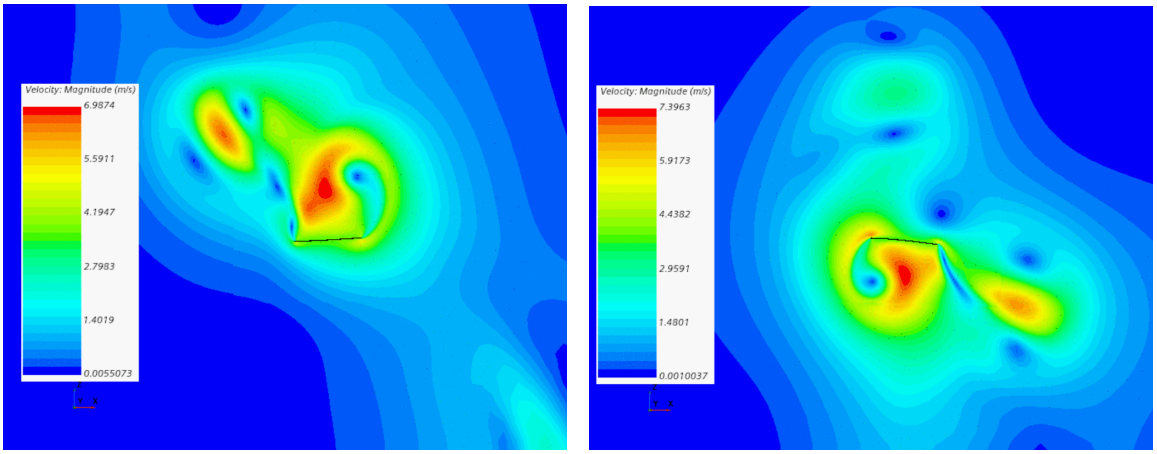

(a) $t^* = 0.25$ (b) $t^* = 0.75$

Fig. 14: Velocity field obtained with the hyperelastic assumption.

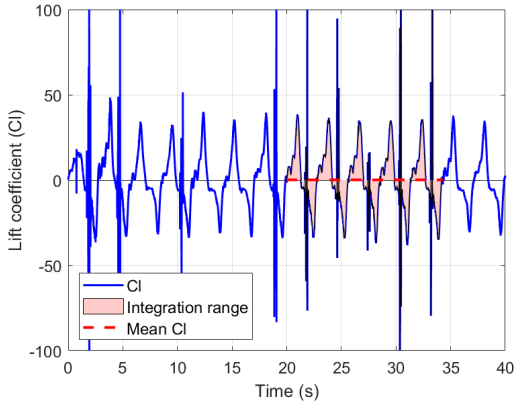

Fig. 15: Lift coefficient obtained for the linear elasticity assumption.

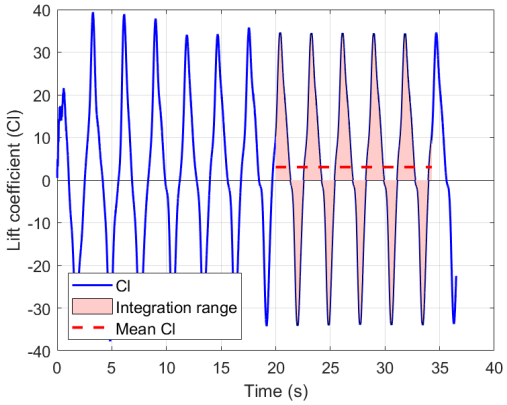

Fig. 16: Lift coefficient obtained for the hyperelasticity assumption.

to flex in the other direction, generating a strong vortex on the underside that generates enough suction to cancel out the average lift coefficient. All this is observed in Figure 13.

When the hyperelastic plate is considered, the plate deformations generate the desired effect: the generation of non-zero lift over a period of the flapping motion of the wing. Figure 20 shows the evolution of the measured lift coefficient throughout the simulation. As can be seen in the figure the time average of this magnitude is non-zero.

Another aspect to be taken into account in both simulations is the frequency with which the aerodynamic coefficients oscillate, as well as their relation to the flow.

The Fourier transforms of the lift coefficient for both cases show that the signal obtained is composed of a single frequency, which coincides with the frequency of the harmonic motion imposed on the leading edge. This is consistent since only each vortex shed by the plate generates an oscillation of the lift generated by the plate, similar to what happens with the flow around a cylinder. However, the Fourier transform of the drag coefficient signal differs in the linear elastic case versus the hyperelastic case. In the linear elastic case, the drag signal is mainly composed of

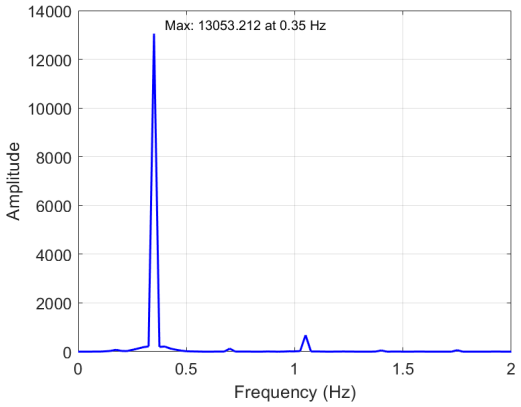

Fig. 17: Fast Fourier Transform with Hann window function for the lift coefficient of the linear elastic case.

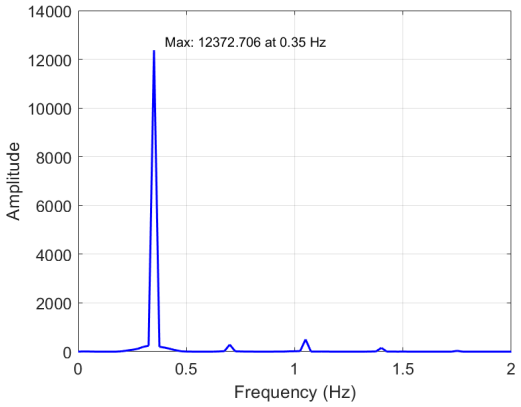

Fig. 18: Fast Fourier Transform with Hann window function for the lift coefficient of the hyperelastic case.

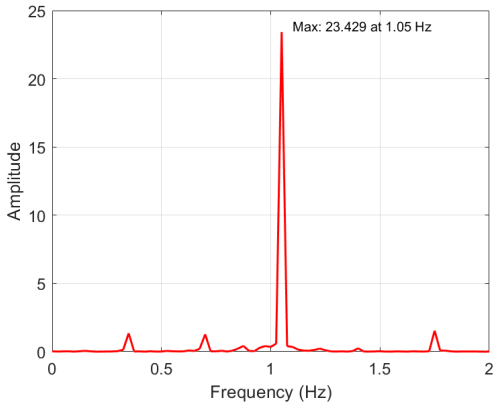

Fig. 19: Fast Fourier Transform with Hann window function for the lift coefficient of the linear elastic case.

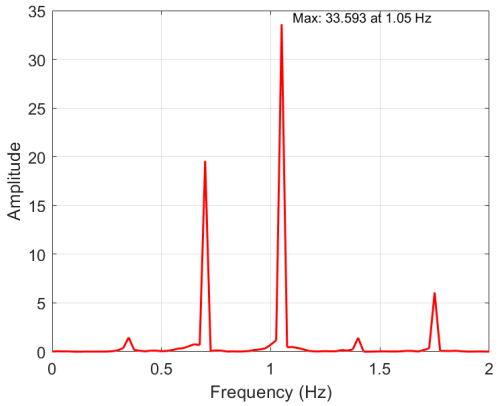

Fig. 20: Fast Fourier Transform with Hann window function for the lift coefficient of the hyperelastic case.

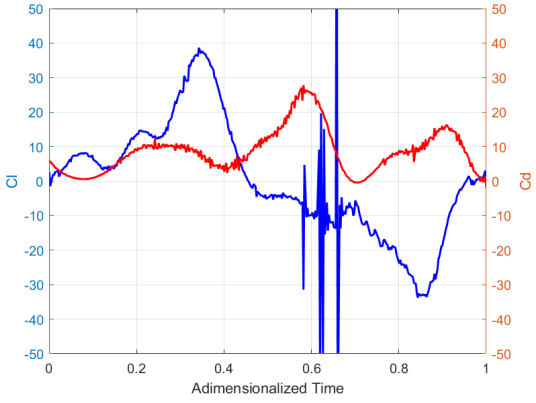

Fig. 21: Evolution of the aerodynamic coefficients over one period under the linear elasticity assumption.

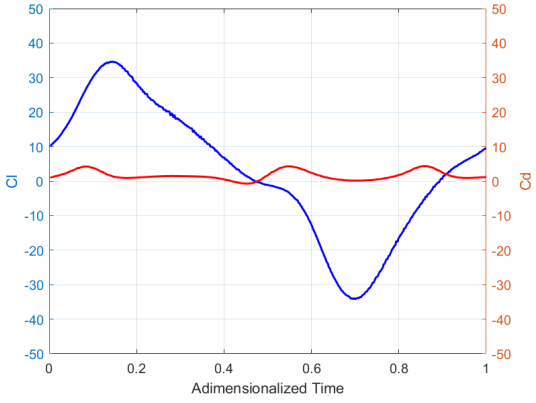

Fig. 22: Evolution of the aerodynamic coefficients over one period under the hyperelastic assumption.

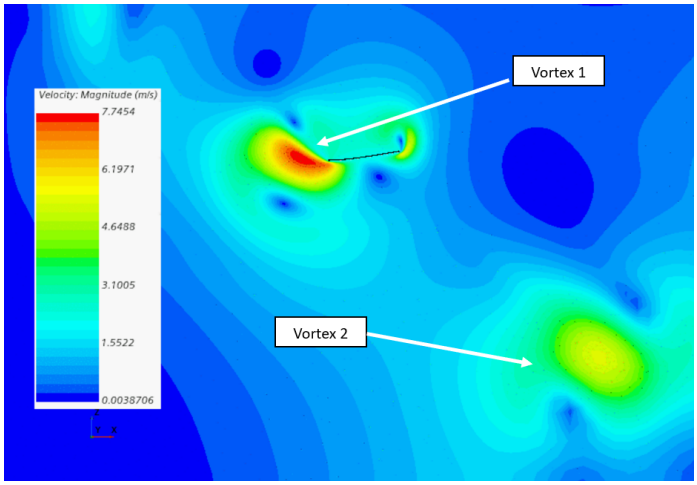

Fig. 23: Vortex shedding observed in the hyperelastic case.

the frequency $f = 1.05$ Hz, which corresponds to three times the frequency of the imposed motion at the leading edge. In the hyperelastic case, the main frequency is the same but has a second component of important contribution for twice the characteristic frequency, $f = 0.7$ Hz.

The explanation for this discrepancy is easily justified when looking at the evolution of the aerodynamic coefficients over one cycle outside the transient period (Figures 21 and 22). As can be seen, the drag coefficient signal has three peaks over one period, as a consequence of how the vortices detach from the plate (Figure 23), while the lift coefficient signal resembles a sinusoidal motion with frequency $f = 0.35$Hz.

IV. Conclusion

In this project, we have discussed the results obtained from simulations of a flexible flat plate subjected to a harmonic motion at its leading edge, intending to understand how certain insects generate lift thanks to the elastic properties of their wings. It has been observed that the linear elasticity hypothesis fails to predict the real behavior of the wing, as the deformations it predicts are outside the range of validity of this hypothesis. It has been necessary to resort to non-linear models (neo-Hookean model) to predict more accurately the results reported in other studies, both numerical and experimental. Although the results with this non-linear model are promising, it is necessary to continue exploring the results that this simulation configuration yields. Therefore, if we were to continue working with this new approach, it would be necessary to carry out mesh convergence and Courant number studies again, to obtain more evident conclusions than those that have been deduced from the linear elasticity simulations. Finally, it would be necessary to analyze different oscillation frequencies, further away from the natural frequency of the plate, to determine how the aerodynamic characteristics of the wing model vary with bending deformations.

References

[1] M. Sridhar, C.-k. K., "Aerodynamic performance of two-dimensional, chordwise flexible flapping wings at fruit fly scale in hover flight," *IOP Science*.

[2] "The aerodynamics of insect flight," .

[3] Kang C-k, S. W., "Scaling law and enhancement of lift generation of a insect-size hovering flexible wing," *Interface*,
doi:https://dx.doi.org/10.1098/rsif.2013.0361.

[4] Kang C-k, c. C. S. W., Aono H, "Effects of flexibility on the aerodynamic performance of flapping wings," *Journal of Fluid Dynamics*,
doi:https://dx.doi.org/10.1017/jgm.2011.428.